HOKKAIDO UNIVERSITY

Title	A Sialylated Voltage-Dependent Ca2+ Channel Binds Hemagglutinin and Mediates Influenza A Virus Entry into Mammalian Cells
Author(s)	Fujioka, Yoichiro; Nishide, Shinya; Ose, Toyoyuki et al.
Citation	Cell host & microbe, 23(6), 809-818 https://doi.org/10.1016/j.chom.2018.04.015
Issue Date	2018-06-13
Doc URL	https://hdl.handle.net/2115/74619
Rights	© 2018. This manuscript version is made available under the CC-BY-NC-ND 4.0 license http://creativecommons.org/licenses/by-nc-nd/4.0/
Rights(URL)	https://creativecommons.org/licenses/by-nc-nd/4.0/
Type	journal article
File Information	CellHostMicrobe23_809.pdf

Hokkaido University Collection of Scholarly and Academic Papers

Hokkaido University Collection of Scholarly and Academic Papers : HUSCAP

Re: CELL-HOST-MICROBE-D-17-00837-R1

A Sialylated Voltage-Dependent Ca^{2+} Channel Binds Hemagglutinin and Mediates Influenza A Virus Entry into Mammalian Cells

Yoichiro Fujioka,[1] Shinya Nishide,[1,7] Toyoyuki Ose,[2,8] Tadaki Suzuki,[3] Izumi Kato,[4] Hideo Fukuhara,[4] Mari Fujioka,[1] Kosui Horiuchi,[1] Aya O. Satoh,[1] Prabha Nepal,[1] Sayaka Kashiwagi,[1] Jing Wang,[1] Mika Horiguchi,[1] Yuko Sato,[3] Sarad Paudel,[1] Asuka Nanbo,[1] Tadaaki Miyazaki,[5] Hideki Hasegawa,[3] Katsumi Maenaka,[2,4] and Yusuke Ohba[1,6,9,*]

[1] Department of Cell Physiology, Faculty of Medicine and Graduate School of Medicine, Hokkaido University, Sapporo 060-8638, Japan

[2] Laboratory of Biomolecular Science Faculty of Pharmaceutical Science, Hokkaido University, Sapporo 060-0812, Japan

[3] Department of Pathology, National Institute of Infectious Diseases, Tokyo 162-0052, Japan

[4] Center for Research and Education on Drug Discovery, Faculty of Pharmaceutical Science, Hokkaido University, Sapporo 060-0812, Japan

[5] Department of Probiotics Immunology, Institute for Genetic Medicine, Hokkaido University, Sapporo 060-0815, Japan

[6] Whitman Center, Marine Biological Laboratory, Woods Hole, MA 02543, USA

[7] Present address: Department of Occupational Therapy, School of Rehabilitation Science, Health Sciences University of Hokkaido, Tobetsu, 061-0293, Japan

[8] Present address: Laboratory of X-ray structural biology, Faculty of Advanced Life Science, Hokkaido University, Sapporo 60-0810, Japan

[9] Lead Contact

*Correspondence: yohba@med.hokudai.ac.jp

Department of Cell Physiology, Faculty of Medicine and Graduate School of Medicine, Hokkaido University, N15W7, Kita-ku, Sapporo 060-8638, Japan.
phone: +81-11-706-5158; fax: +81-11-706-7877

SUMMARY

Influenza A virus (IAV) infection is initiated by the attachment of the viral glycoprotein hemagglutinin (HA) to sialic acid on the host cell surface. However, the sialic acid–containing receptor crucial for IAV infection has remained unidentified. Here we show that HA binds to the voltage-dependent Ca^{2+} channel $Ca_v1.2$ to trigger intracellular Ca^{2+} oscillations and subsequent IAV entry and replication. IAV entry was inhibited by Ca^{2+} channel blockers (CCBs) or by knockdown of $Ca_v1.2$. The CCB diltiazem also inhibited virus replication *in vivo*. Reintroduction of wild-type but not the glycosylation-deficient mutants of $Ca_v1.2$ restored Ca^{2+} oscillations and virus infection in $Ca_v1.2$-depleted cells, demonstrating the significance of $Ca_v1.2$ sialylation. Taken together, we identify $Ca_v1.2$ as a sialylated host cell surface receptor that binds HA and is critical for IAV entry.

INTRODUCTION

Influenza is a human respiratory infection caused by influenza viruses, and spreads worldwide in an annual outbreak or does occasionally in pandemics, resulting in significant morbidity and mortality (Herfst et al., 2012). The primary event in influenza virus infection is the attachment of virus particles to the host cell surface, which is mediated by the binding of HA to sialylated cell surface receptors on respiratory or intestinal epithelial cells in humans and birds, respectively (Kumlin et al., 2008). Avian viruses bind preferentially to receptors with α2,3-linked sialic acid moieties, whereas human-adapted viruses are specific for the α2,6 linkage (Connor et al., 1994; Rogers and D'Souza, 1989). This specificity is key to determination of the host range of each viral strain. Given that the sialic acid that contributes to the binding of HA to the cell surface may be presented on a glycoprotein, many studies have attempted to identify specific IAV receptor protein(s). Such identified proteins include the killer-activating proteins NKp44 and NKp46 in natural killer cells (Achdout et al., 2010; Arnon et al., 2004; Ho et al., 2008; Mandelboim et al., 2001), as well as the epidermal growth factor receptor in lung epithelial cells (Eierhoff et al., 2010). However, the binding of IAV to sialylated cell surface proteins does not always result in receptor-mediated internalization (Carroll and Paulson, 1985; Williams and Robertson, 1993), suggesting that the engagement of specific cellular signaling may be required to initiate virus endocytosis.

IAVs enter host cells via redundant endocytic pathways, including clathrin-mediated endocytosis, clathrin-independent endocytosis, and Macropinocytosis (Chen and Zhuang,

2008; Doxsey et al., 1987; Fujioka et al., 2011; 2013; Matlin et al., 1981; Rust et al., 2004; Sieczkarski and Whittaker, 2002). It has been previously demonstrated that intracellular Ca^{2+} plays a central role in upregulating such endocytic pathways (Fujioka et al., 2013). Indeed, IAV infection induces Ca^{2+} oscillations of host cells, and the infection is markedly attenuated by the chelation of both intracellular and extracellular Ca^{2+} by BAPTA-AM and EGTA, respectively (Fujioka et al., 2013), suggesting that Ca^{2+} flux from the outside to the inside of cell may also play a role in the regulation of IAV entry and infection.

The intracellular calcium ion concentration ($[Ca^{2+}]_i$) is normally maintained at a low level by various membrane transporters including Na^+-Ca^{2+} exchangers and Ca^{2+}-dependent ATPases at the plasma membrane, sarco-endoplasmic reticulum Ca^{2+}-ATPases (SERCAs) and a Ca^{2+}-H^+ exchanger in mitochondria as well as by cytoplasmic Ca^{2+}-binding proteins (Berridge et al., 2003). Cell stimulation with various ligands triggers an increase in $[Ca^{2+}]_i$ that results from the activation of Ca^{2+} channels including voltage-dependent calcium channels (VDCCs), inositol 1,4,5-trisphosphate (IP_3)-gated Ca^{2+} channels and ryanodine receptors. Among them, VDCCs might be a candidate that mediate the IAV-induced increase in $[Ca^{2+}]_i$ in host cells, because (1) these channels are expressed at the plasma membrane, (2) their function is modified by sialylation (Ednie and Bennett, 2012), (3) one of the calcium channel blockers (CCBs), verapamil, inhibits IAV replication by an unknown mechanism (Nugent and Shanley, 1984) and (4) extracellular Ca^{2+} is also important for the IAV-induced increase in $[Ca^{2+}]_i$ (Fujioka et al., 2013). In this study, we demonstrated that the VDCC $Ca_v1.2$ (encoded by the *CACNA1C* gene) bound to IAV HA. The binding through sialic acid was crucial for IAV infection, entry, and IAV-induced Ca^{2+} oscillation. The effect of the CCBs on virus infection was also demonstrated *in vitro, ex vivo,* and *in vivo*. Taken together, our analysis revealed that $Ca_v1.2$ acts as a key cell surface molecule for IAVs to hijack host cell machinery of endocytosis for their efficient incorporation into host cells.

RESULTS

CCBs Suppress IAV Replication, IAV Internalization, and IAV-Induced Ca^{2+} Oscillations

To test whether VDCCs play a role in IAV infection, we first evaluated the effect of CCBs on the plaque-forming activity of the IAV strains A/Puerto Rico/8/34 (H1N1; PR8) in Madin-Darby canine kidney (MDCK) cells. All tested CCBs, including amlodipine, verapamil, and diltiazem, as well as BAPTA-AM, inhibited IAV replication in a dose-dependent manner (**Figure S1A**). Based on their IC_{95} values, amlodipine, verapamil, diltiazem, and BAPTA-AM were used at concentrations of 25, 50, 200, 25 μM, respectively, in the following experiments. Of note, treatment with drugs at these concentrations displayed no significant toxicity in MDCK cells (**Figure S1B**). The treatment with CCBs resulted in inhibition of replication of both PR8 and A/Aichi/2/68 (H3N2; Aichi) with the exception that verapamil did not significantly inhibit infection with the Aichi strain ($P = 0.0512$) (**Figures 1A** and **1B**). Given that the inhibitory effect of diltiazem was the most pronounced and was similar to that of the intracellular Ca^{2+} chelator BAPTA-AM, which was previously shown to be an effective inhibitor of IAV infection (Fujioka et al., 2013), we chose this reagent for subsequent experiments. Next, to further evaluate the effect of CCBs on IAV infection in other mammalian cells than MDCK cells, we utilized immunofluorescence-based infection assay. This assay visualizes single-round replication at a single cell level (**Figure S1C**), and the percentage of NP-positive cells is correlated with the titer of infected viruses (**Figure S1D**), thereby expanding cell strains that can be analyzed. With this assay, we noticed that diltiazem also inhibited infection of PR8 in A549, MDCK, 293T, and Cos-1 cells (**Figures 1C** and **S1E**) without remarkable cytotoxicity (**Figure S1F**). We next examined the effect of diltiazem on IAV-induced Ca^{2+} oscillations with the use of the Förster resonance energy transfer (FRET)-based Ca^{2+} sensor Yellow Cameleon (YC3.60) (Nagai et al., 2004) and found that it inhibited PR8- or Aichi-induced Ca^{2+} oscillations in both Cos-1 and A549 cells (**Figures 1D**, **1E**, **S1G**, and **S1H; Supplementary Movies 1**, **2**). Moreover, diltiazem also inhibited virus internalization (**Figures 1F** and **1G**). Together, these results indicated that VDCCs contribute to IAV entry and subsequent infection.

Knockdown of $Ca_v1.2$ Inhibits IAV-Induced Ca^{2+} Oscillations, IAV Internalization, and IAV Infection

Among VDCC family members (L-, P/Q-, N-, R- and T-type channels), L-type VDCCs are expressed ubiquitously, including respiratory epithelia (Brennan et al., 2013), whereas non–L-

type channels show neuron- or sinus node-restricted expression patterns (Catterall, 2011; Catterall et al., 2005). In addition, among L-type channels, whereas $Ca_v1.2$ expression has been detected in a range of tissues, $Ca_v1.1$, $Ca_v1.3$ and $Ca_v1.4$ are expressed predominantly in skeletal muscle, neuroendocrine tissues and the retina, respectively (Catterall et al., 2005). The copy number of $Ca_v1.2$ mRNA was markedly higher than that of $Ca_v1.1$, $Ca_v1.3$ or $Ca_v1.4$ mRNAs in the human cell lines examined in the present study (**Figure S2A**). Knockdown of $Ca_v1.2$ (by up to ~60% as revealed by immunoblot analysis) (**Figure S2B**) in A549 cells by transfection with small interfering RNAs (siRNAs) inhibited PR8-induced Ca^{2+} oscillations, virus entry, and virus infection (**Figures 2A–C**). In addition, $Ca_v1.2$ knockdown inhibited PR8-induced Ca^{2+} oscillations as well as PR8 infection in 293T cells (**Figures S2C** and **D**). Furthermore, progeny virus production in $Ca_v1.2$-knockdown 293T cells was found to be inhibited, as evaluated by an MDCK plaque assay (**Figure S2E**). These results together indicated that the observed inhibitory effects of CCBs were not due to off-target actions and that $Ca_v1.2$ contributes to IAV infection in multiple cell contexts.

HA Binds to $Ca_v1.2$

To explore the molecular mechanism by which IAV activates $Ca_v1.2$, we exposed cells expressing YC3.60 to PR8 labeled with the lipophilic tracer DiD and then imaged them by time-lapse microscopy every 2 s. This approach allowed the monitoring of Ca^{2+} dynamics at virus attachment sites with high temporal resolution. Transient small increases in $[Ca^{2+}]_i$ around some of the regions at which virus particles had adsorbed were detected before the robust increase in $[Ca^{2+}]_i$ apparent throughout the entire cell (**Figures S3A–C**), suggesting that IAV might directly bind to and activate $Ca_v1.2$. To test this possibility, we performed a membrane binding assay (Côté et al., 2011) with a membrane fraction prepared from cells expressing either full-length $Ca_v1.2$ or fragments thereof (**Figures 3A** and **3B**). We found that PR8 bound to full-length (FL) $Ca_v1.2$ (**Figure 3C**) and that this binding was partially inhibited by treatment with sialidase but not by the Ca^{2+} chelator EGTA (**Figure 3C**). These results indicated that sialylation of $Ca_v1.2$ is required for IAV binding, whereas Ca^{2+} is dispensable. Analysis of membrane fractions of cells expressing truncation mutants of $Ca_v1.2$ revealed that IAV preferentially bound to fragment containing segment IV of $Ca_v1.2$ (**Figure 3D**). It was recently reported that there are two potential sialylated asparagine residues (N1436 and N1487) in segment IV (Lazniewska and Weiss, 2017) (**Figure 3B**), suggesting that the HA glycoprotein might be responsible for binding of IAV to this fragment. To test this notion more directly, we performed a co-immunoprecipitation assay for HA and $Ca_v1.2$.

HA is retained at the plasma membrane or virus surface through the transmembrane region at its COOH-terminus (Mair et al., 2014), and trimer formation by HA determines the rate of its transport for secretion (Ceriotti and Colman, 1990). We therefore constructed an expression vector for a form of HA in which the transmembrane region is replaced with a six-histidine (6×His) tag and a foldon domain, a natural trimerization domain from T4 bacteriophage fibritin (Meier et al., 2004) (**Figure S3D**). The modified HA protein (HA-His) would be expected to be secreted from cells as a trimer and to contact the cell surface region of $Ca_v1.2$. As expected, HA-His was detected in immunoprecipitates of full-length (FL) $Ca_v1.2$ or of fragment III-IV, but not in those of fragment I-II (**Figures 3E** and **3F**). Given that the membrane-localized fraction of truncation mutants was comparable to that of full-length $Ca_v1.2$ (**Figure S3E**), the difference in precipitation might be accounted for by the difference in binding affinity to HA, but not by their localization. The binding of HA to fragment III-IV was partially inhibited by treatment with sialidase, suggesting that HA indeed binds to segment IV (or III) of $Ca_v1.2$ through sialylated residues (**Figure S3F**).

HA Bindings to $Ca_v1.2$ through Glycosylated Asparagine Residues is Crucial for Calcium Oscillation and Virus Infection

To examine further whether sialylation of $Ca_v1.2$ is required for the HA-$Ca_v1.2$ interaction, we constructed $Ca_v1.2$ mutants in which one or both of the potential sialylated asparagine residues in domain IV was replaced with glutamine (N1436Q, N1487Q and N1436Q + N1487Q). Expression of the wild-type form of fragment III-IV of $Ca_v1.2$ in 293T cells gave rise to two distinct bands, only the faster migrating of which was detected in cells expressing the mutants (**Figure S4A**). This result suggested that the slower migrating band (indicated by arrowhead) represented a form of the fragment that was glycosylated at N1436, N1487, or both residues. Indeed, the upper band of the wild-type fragment was no longer evident after treatment with peptide:N-glycosidase F (PNGase F), which inhibits IAV infection (Chu and Whittaker, 2004), whereas such treatment had no effect on the electrophoretic mobility of the mutants (**Figure S4B**). The binding of HA to the $Ca_v1.2$ mutants was attenuated compared with that apparent with the wild-type fragment (**Figure 4A**). The extent of this attenuation was similar to that induced by sialidase treatment (**Figures 3C** and **S3F**), suggesting that sialic acid-dependent binding of $Ca_v1.2$ to HA might be dictated by these asparagine residues.

To provide more evidence for this notion, we performed rescue experiments, in which wild-type $Ca_v1.2$ or its glycosylation-deficient N1436Q + N1487Q mutant was introduced into A549 cells that had been depleted of endogenous $Ca_v1.2$ by transfection with an siRNA

(siCav1.2#13) targeted to the 3' untranslated region of $Ca_v1.2$ mRNA. Whereas wild-type $Ca_v1.2$ restored single-round infection with IAV in the $Ca_v1.2$ knockdown cells, the mutant failed to do so (**Figure 4B**). Moreover, wild-type $Ca_v1.2$, but not the mutant protein, restored PR8-induced Ca^{2+} oscillations in the knockdown cells (**Figure S4C**). Given that the glycosylation deficient mutant could be localized at the plasma membrane to a similar extent as the wild-type form (**Figure S4D**), it was indicated that glycosylation at N1436 or N1487 (or both residues) of $Ca_v1.2$ and the binding of these residues to HA are critical for Ca^{2+}-regulated virus infection.

The CCB Diltiazem Inhibits IAV Infection *In Vivo* and *Ex Vivo*.

To demonstrate the significance of VDCCs and its inhibition in IAV infection *in vivo*, we first confirmed that VDCC proteins were indeed expressed in viral target cells in the murine respiratory tissues by immunohistochemistry. Epithelia in the nasal cavity, trachea, and bronchioles, as well as alveolar macrophages were positive for the viral antigen NP protein (**Figures 5A**–**D**). In these cells, Ca_v proteins were shown to be expressed despite the difference in their abundance (**Figures 5A**–**D**), suggesting that Ca_v proteins are present in viral target cells in respiratory tissues and might be involved in IAV infection.

Under this condition, we examined the effect of the CCB diltiazem on IAV infection *in vivo*. Given that oral or intraperitoneal administration of diltiazem does not result in delivery of the drug to respiratory tissues (Sun et al., 2009), we administered PR8 (50 PFU) to anesthetized mice intranasally, treated the animals with diltiazem intranasally beginning either before or after virus exposure and examined the effect of the drug on viral replication in the nasal cavity (**Figure 6A**). Prophylactic administration of diltiazem resulted in a significant and dose-dependent reduction in the viral amount of nasal lavage fluid (**Figures 6B** and **S5A**); although this effect was less pronounced than that of the anti-influenza drug oseltamivir, the difference in the observed maximal effects of the two drugs was not significant. Diltiazem also inhibited virus replication when the treatment was initiated 1 day after exposure to PR8 (**Figure 6C**), with this effect being similar to that of oseltamivir. To further demonstrate the effectiveness of CCB to protect against lethal infection, mice were challenged with a higher dose of PR8 (10^4 PFU) and monitored for survival and body weight changes (**Figures 6D** and **6E**). Diltiazem administration significantly prolonged survival and allowed the recovery of the survivors. Taken together, the CCB was thus effective as both a prophylactic and therapeutic agent to a wide range of doses of infection.

We also evaluated the effect of diltiazem on IAV infection to human respiratory epithelial cells. To this aim, the human bronchial epithelial cell line BEAS-2B was recruited. BEAS-2B cells were known to form spheroid (mimics of alveoli) and epithelial monolayer (mimics of bronchial epithelium) when cultured “on” and “in” Matrigel (Shen et al., 2015). After formation of either spheroid (**Figure S5B**) or monolayer (**Figure S5C**), the cells were then pre-treated with diltiazem and exposed to PR8. In both structures, IAV NP-positive cells were dramatically decreased by the treatment, affirming that the CCB was also effective human respiratory epithelial cells.

DISCUSSION

In this study, we have shown that $Ca_v1.2$ bound to IAV HA and functional analysis also revealed that $Ca_v1.2$ and its binding to HA through sialic acid were involved in IAV infection and IAV-induced Ca^{2+} oscillation. These observations together demonstrated $Ca_v1.2$ as one of the key cell surface molecules for IAVs to hijack host cell machinery for their efficient incorporation into cells and subsequent infection. Given that the sequence of sialic acid binding site of HA is highly conserved across the serotypes, whereas antigen drift is frequently observed in other parts, the findings presented here are expected to lead to the development of a novel approach to inhibit IAV infection by targeting the HA-calcium channel interaction. Such therapeutics appears to be effective to a range of serotypes and tolerant to drug resistant strains.

Extensive studies have been performed to identify sialylated cell surface proteins that mediate the virus-host cell interaction via binding to HA protein over the past years (Achdout et al., 2010; Arnon et al., 2004; Eierhoff et al., 2010; Ho et al., 2008; Mandelboim et al., 2001). However, no protein has been identified as a key host cell receptor for IAV so far; that is, the viruses still infect cells even in the presence of inhibitors for respective molecules or in the absence of the target molecules through knockdown experiments (Eierhoff et al., 2010). Therefore, identification of a protein(s) that is critical for IAV adsorption to host cells and subsequent infection has yet to be eagerly anticipated. One of the reason why such a wide variety of proteins are identified as a binding partner for HA, but are not involved in IAV entry and infection, might be accounted partly for by the abundance of sialylated proteins on the cell surface; viz. when there is an abundant protein that is modified by α2,3-linked or α2,6-linked sialic acids at many sites and is irrelevant to IAV infection, the sensitivity to detect the real targets can be decreased markedly. Another possible reason that makes molecular identification difficult might be accounted for by non-specific or sialic acid-independent binding to HA. In this study, binding of glycosylation-deficient mutants of $Ca_v1.2$ was significantly reduced (by ~40%) than that of wild type, but not abolished completely (**Figure 4A**), suggesting that $Ca_v1.2$ may also bind to HA at multiple extracellular regions in a manner independent of sialic acid. Accordingly, sialidase treatment also displayed partial inhibitory effect on the binding (**Figures 3C** and **S3F**).

Although we here show that IAV bound to N1436 and N1487 residues in segment IV of $Ca_v1.2$ to evoke host cell Ca^{2+} signaling and facilitate infection (**Figures 4B** and **S4C**), the molecular mechanism through which the binding induces Ca^{2+} influx has not been clarified.

The possible mechanisms include: 1) an increase in channel conductance, 2) an increase in opening probability of the channel, and 3) decreased interaction of α1 and other subunits. Several reports implicate glycosylation of calcium channels in their function. For example, $Ca_v1.2$, is glycosylated at two asparagine residues in domain I in addition to N1436 and N1487 in domain IV (Lazniewska and Weiss, 2017), and mutation in the asparagine residues in domain I caused a depolarizing shift in voltage-dependent gating of rabbit $Ca_v1.2$ (Park et al., 2015). Furthermore, glycosylation at asparagine N192 and N1466 in segments I and III of the human low-voltage-gated T-type calcium $Ca_v3.2$ plays an essential role in the conducting function by enhancing the permeability and/or the pore opening of the channel (Ondacova et al., 2016). Therefore, it is possible that binding of HA to asparagine residues through sugar chains modulates channel functions, although glycosylation in segment IV *per se* does not affect voltage-dependent gating (Park et al., 2015).

VDCC is a multimeric complex that consists of α1, α2, β, δ, and γ (Catterall, 2011; Catterall et al., 2005). In particular, interaction of α1 subunit to β subunit through highly conserved α-interaction domain within the cytoplasmic loop between the domains I and II of α1 subunit is critical in determining VDCCs properties, including channel gating (Budde et al., 2002; Buraei and Yang, 2013). Given that the interaction with β subunits often suppresses channel activity through shift of the voltage dependence to more hyperpolarized voltages and promotion of voltage-dependent inactivation (Dolphin, 2012; Meir et al., 2000), it is therefore possible that binding of HA to $Ca_v1.2$ interferes the interaction and activates VDCCs through derepression.

$Ca_v1.2$ contains consensus sequences for glycosylation with N-linked glycan (N-X-T) at 1436 and 1487 in the domain IV (Lazniewska and Weiss, 2017), and glycosylation at these asparagine residues were demonstrated to be important for IAV-induced $[Ca^{2+}]_i$ increase (**Figure S4C**). Such N-glycosylation sites are not conserved in other VDCC isoforms except for $Ca_v2.2$, which possesses a potentially sialylated asparagine residue (N1675) in the segment IV (Lazniewska and Weiss, 2017). Regarding other type of channels, there exist a large number of possible glycosylated asparagine residues (Lazniewska and Weiss, 2017). Although significance of glycosylation at these sites is unclear, it is therefore possible that the sialylated channels other than $Ca_v1.2$ also bind to HA and play a role in influenza virus infection. Nevertheless, given the tissue or cell-type restricted expression pattern of other types of channels than $Ca_v1.2$, global significance of the contribution of such channels should be further demonstrated in the future.

ACKNOWLEDGEMENTS

We thank A. Miyawaki and T. Nagai for expression plasmids, K. Kihatsu for cDNA for HA of PR8, and A. Kikuchi for technical assistance. This work was supported in part by Grants-in-Aid from the Ministry of Education, Culture, Sports, Science and Technology of Japan (#26115701 and #15H01248), from the Japan Society for the Promotion of Science (#26293041 and #16H06227), and from the Japan Agency for Medical Research and Development (JP17fk0108124j0601), as well as by grants from Mochida Memorial Foundation for Medical and Pharmaceutical Research, the Waksman Foundation of Japan, the Sumitomo Electric Group Corporate Social Responsibility Foundation, and SENSHIN Medical Research Foundation.

AUTHOR CONTRIBUTIONS

Conceptualization, Y.F., S.P, and Y.O.; Methodology, Y.F. and A.N.; Formal Analysis, S.N.; Investigation, S.N., T.O., T.S., I.K., H.F., K.H., A.O.S., P.N., S.K., J.W., M.H., and Y.S.; Resources, T.O., I.K., H.F., M.F., T.M. and K.M.; Writing – Original Draft, Y.F. and Y.O.; Writing – Review & Editing, Y.F., T.S., S.P. and Y.O.; Visualization, Y.F., T.S., H.H., and Y.O.; Supervision, T.M., H.H., K.M., and Y.O.; Project Administration, Y.O.; Funding Acquisition, Y.F., T.S., H.H., and Y.O.

DECLARATION OF INTERESTS

A patent includes in part claims relating to CCB has been filed by Hokkaido University with Y.O. and T.M. as co-inventors. Other authors declare no conflicts of interest.

REFERENCES

Achdout, H., Meningher, T., Hirsh, S., Glasner, A., Bar-On, Y., Gur, C., Porgador, A., Mendelson, M., Mandelboim, M., and Mandelboim, O. (2010). Killing of avian and Swine influenza virus by natural killer cells. J. Virol. *84*, 3993–4001.

Arnon, T.I., Achdout, H., Lieberman, N., Gazit, R., Gonen-Gross, T., Katz, G., Bar-Ilan, A., Bloushtain, N., Lev, M., Joseph, A., et al. (2004). The mechanisms controlling the recognition of tumor- and virus-infected cells by NKp46. Blood *103*, 664–672.

Berridge, M.J., Bootman, M.D., and Roderick, H.L. (2003). Calcium signalling: dynamics, homeostasis and remodelling. Nat. Rev. Mol. Cell. Biol. *4*, 517–529.

Brennan, S.C., Finney, B.A., Lazarou, M., Rosser, A.E., Scherf, C., Adriaensen, D., Kemp, P.J., and Riccardi, D. (2013). Fetal calcium regulates branching morphogenesis in the developing human and mouse lung: involvement of voltage-gated calcium channels. PLoS ONE *8*, e80294.

Budde, T., Meuth, S., and Pape, H.-C. (2002). Calcium-dependent inactivation of neuronal calcium channels. Nat. Rev. Neurosci. *3*, 873–883.

Buraei, Z., and Yang, J. (2013). Structure and function of the beta subunit of voltage-gated Ca^{2+} channels. Biochim. Biophys. Acta *1828*, 1530–1540.

Carroll, S.M., and Paulson, J.C. (1985). Differential infection of receptor-modified host cells by receptor-specific influenza viruses. Virus Res. *3*, 165–179.

Catterall, W.A. (2011). Voltage-gated calcium channels. Cold Spring Harb. Perspect. Biol. *3*, a003947.

Catterall, W.A., Perez-Reyes, E., Snutch, T.P., and Striessnig, J. (2005). International Union of Pharmacology. XLVIII. Nomenclature and structure-function relationships of voltage-gated calcium channels. Pharmacol. Rev. *57*, 411–425.

Ceriotti, A., and Colman, A. (1990). Trimer formation determines the rate of influenza virus haemagglutinin transport in the early stages of secretion in Xenopus oocytes. J. Cell Biol. *111*, 409–420.

Chen, C., and Zhuang, X. (2008). Epsin 1 is a cargo-specific adaptor for the clathrin-mediated endocytosis of the influenza virus. Proc. Natl Acad. Sci. USA *105*, 11790–11795.

Chu, V.C., and Whittaker, G.R. (2004). Influenza virus entry and infection require host cell N-linked glycoprotein. Proc. Natl Acad. Sci. USA *101*, 18153–18158.

Connor, R.J., Kawaoka, Y., Webster, R.G., and Paulson, J.C. (1994). Receptor specificity in human, avian, and equine H2 and H3 influenza virus isolates. Virology *205*, 17–23.

Côté, M., Misasi, J., Ren, T., Bruchez, A., Lee, K., Filone, C.M., Hensley, L., Li, Q., Ory, D., Chandran, K., et al. (2011). Small molecule inhibitors reveal Niemann-Pick C1 is essential for Ebola virus infection. Nature *477*, 344–348.

Dolphin, A.C. (2012). Calcium channel auxiliary α2δ and β subunits: trafficking and one step beyond. Nat. Rev. Neurosci. *13*, 542–555.

Doxsey, S.J., Brodsky, F.M., Blank, G.S., and Helenius, A. (1987). Inhibition of endocytosis by anti-clathrin antibodies. Cell *50*, 453–463.

Edenborough, K.M., Gilbertson, B.P., and Brown, L.E. (2012). A mouse model for the study of contact-dependent transmission of influenza A virus and the factors that govern transmissibility. J. Virol. *86*, 12544–12551.

Ednie, A.R., and Bennett, E.S. (2012). Modulation of voltage-gated ion channels by sialylation. Compr. Physiol. *2*, 1269–1301.

Eierhoff, T., Hrincius, E.R., Rescher, U., Ludwig, S., and Ehrhardt, C. (2010). The epidermal growth factor receptor (EGFR) promotes uptake of influenza A viruses (IAV) into host cells. PLoS Pathog. *6*, e1001099.

Fujioka, Y., Tsuda, M., Hattori, T., Sasaki, J., Sasaki, T., Miyazaki, T., and Ohba, Y. (2011). The Ras-PI3K signaling pathway is involved in clathrin-independent endocytosis and the internalization of influenza viruses. PLoS ONE *6*, e16324.

Fujioka, Y., Tsuda, M., Nanbo, A., Hattori, T., Sasaki, J., Sasaki, T., Miyazaki, T., and Ohba, Y. (2013). A Ca^{2+}-dependent signalling circuit regulates influenza A virus internalization and infection. Nat. Commun. *4*, 2763.

Herfst, S., Schrauwen, E.J., Linster, M., Chutinimitkul, S., de Wit, E., Munster, V.J., Sorrell, E.M., Bestebroer, T.M., Burke, D.F., Smith, D.J., et al. (2012). Airborne transmission of influenza A/H5N1 virus between ferrets. Science *336*, 1534–1541.

Ho, J.W., Hershkovitz, O., Peiris, M., Zilka, A., Bar-Ilan, A., Nal, B., Chu, K., Kudelko, M., Kam, Y.W., Achdout, H., et al. (2008). H5-type influenza virus hemagglutinin is functionally recognized by the natural killer-activating receptor NKp44. J. Virol. *82*, 2028–2032.

Horiguchi, M., Fujioka, M., Kondo, T., Fujioka, Y., Li, X., Horiuchi, K., O Satoh, A., Nepal, P., Nishide, S., Nanbo, A., et al. (2017). Improved FRET biosensor for the measurement of BCR-ABL activity in chronic myeloid leukemia cells. Cell Struct. Funct. *42*, 15–26.

Iwasaki, T., Tamura, S., Kumasaka, T., Sato, Y., Hasegawa, H., Asanuma, H., Aizawa, S., Yanagihara, R., and Kurata, T. (1999). Exacerbation of influenzavirus pneumonia by intranasal administration of surfactant in a mouse model. Arch. Virol. *144*, 675–685.

Kumlin, U., Olofsson, S., Dimock, K., and Arnberg, N. (2008). Sialic acid tissue distribution and influenza virus tropism. Influenza Other Respir. Viruses *2*, 147–154.

Lazniewska, J., and Weiss, N. (2017). Glycosylation of voltage-gated calcium channels in health and disease. Biochim. Biophys. Acta *1859*, 662–668.

Mair, C.M., Ludwig, K., Herrmann, A., and Sieben, C. (2014). Receptor binding and pH stability - how influenza A virus hemagglutinin affects host-specific virus infection. Biochim. Biophys. Acta *1838*, 1153–1168.

Mandelboim, O., Lieberman, N., Lev, M., Paul, L., Arnon, T.I., Bushkin, Y., Davis, D.M., Strominger, J.L., Yewdell, J.W., and Porgador, A. (2001). Recognition of haemagglutinins on virus-infected cells by NKp46 activates lysis by human NK cells. Nature *409*, 1055–1060.

Matlin, K.S., Reggio, H., Helenius, A., and Simons, K. (1981). Infectious entry pathway of influenza virus in a canine kidney cell line. J. Cell Biol. *91*, 601–613.

Meier, S., Güthe, S., Kiefhaber, T., and Grzesiek, S. (2004). Foldon, the natural trimerization domain of T4 fibritin, dissociates into a monomeric A-state form containing a stable beta-hairpin: atomic details of trimer dissociation and local beta-hairpin stability from residual dipolar couplings. J. Mol. Biol. *344*, 1051–1069.

Meir, A., Bell, D.C., Stephens, G.J., Page, K.M., and Dolphin, A.C. (2000). Calcium channel β subunit promotes voltage-dependent modulation of α1B by Gβγ. Biophys. J. *79*, 731–746.

Nagai, T., Yamada, S., Tominaga, T., Ichikawa, M., and Miyawaki, A. (2004). Expanded dynamic range of fluorescent indicators for Ca^{2+} by circularly permuted yellow fluorescent proteins. Proc. Natl Acad. Sci. USA *101*, 10554–10559.

Nanbo, A., Imai, M., Watanabe, S., Noda, T., Takahashi, K., Neumann, G., Halfmann, P., Kawaoka, Y. (2010). Ebolavirus is internalized into host cells via macropinocytosis in a viral glycoprotein-dependent manner. PLoS Pathog. *6*, e1001121.

Ng, W.C., Wong, V., Muller, B., Rawlin, G., and Brown, L.E. (2010). Prevention and treatment of influenza with hyperimmune bovine colostrum antibody. PLoS ONE *5*, e13622.

Nugent, K.M., and Shanley, J.D. (1984). Verapamil inhibits influenza A virus replication. Arch. Virol. *81*, 163–170.

Ohba, Y., Kurokawa, K., and Matsuda, M. (2003). Mechanism of the spatio-temporal regulation of Ras and Rap1. EMBO J. *22*, 859–869.

Ondacova, K., Karmazinova, M., Lazniewska, J., Weiss, N., and Lacinova, L. (2016). Modulation of $Cav_{3.2}$ T-type calcium channel permeability by asparagine-linked glycosylation. Channels *10*, 175–184.

Park, H.-J., Min, S.-H., Won, Y.-J., and Lee, J.-H. (2015). Asn-Linked Glycosylation Contributes to Surface Expression and Voltage-Dependent Gating of Cav1.2 Ca^{2+} Channel. J. Microbiol. Biotechnol. *25*, 1371–1379.

Pleschka, S., Wolff, T., Ehrhardt, C., Hobom, G., Planz, O., Rapp, U., and Ludwig, S. (2001). Influenza virus propagation is impaired by inhibition of the Raf/MEK/ERK signalling cascade. Nat. Cell Biol. *3*, 301–305.

Rogers, G.N., and D'Souza, B.L. (1989). Receptor binding properties of human and animal H1 influenza virus isolates. Virology *173*, 317–322.

Rust, M.J., Lakadamyali, M., Zhang, F., and Zhuang, X. (2004). Assembly of endocytic machinery around individual influenza viruses during viral entry. Nat. Struct. Mol. Biol. *11*, 567–573.

Shen, Y., Hou, Y., Yao, S., Huang, P., and Yobas, L. (2015). In vitro epithelial organoid generation induced by substrate nanotopography. Sci. Rep. *5*, 9293.

Sieczkarski, S.B., and Whittaker, G.R. (2002). Influenza virus can enter and infect cells in the absence of clathrin-mediated endocytosis. J. Virol. *76*, 10455–10464.

Sun, Y., Liou, B., Quinn, B., Ran, H., Xu, Y.-H., and Grabowski, G.A. (2009). In vivo and ex vivo evaluation of L-type calcium channel blockers on acid beta-glucosidase in Gaucher disease mouse models. PLoS ONE *4*, e7320.

Takeda, M., Ohno, S., Seki, F., Nakatsu, Y., Tahara, M., and Yanagi, Y. (2005). Long untranslated regions of the measles virus M and F genes control virus replication and cytopathogenicity. J. Virol. *79*, 14346–14354.

Tomosugi, W., Matsuda, T., Tani, T., Nemoto, T., Kotera, I., Saito, K., Horikawa, K., and Nagai, T. (2009). An ultramarine fluorescent protein with increased photostability and pH insensitivity. Nat. Methods *6*, 351–353.

Williams, S.P., and Robertson, J.S. (1993). Analysis of the restriction to the growth of nonegg-adapted human influenza virus in eggs. Virology *196*, 660–665.

Yoshida, R., Igarashi, M., Ozaki, H., Kishida, N., Tomabechi, D., Kida, H., Ito, K., and Takada, A. (2009). Cross-protective potential of a novel monoclonal antibody directed against antigenic site B of the hemagglutinin of influenza A viruses. PLoS Pathog. *5*, e1000350.

FIGURE LEGENDS

Figure 1. Pharmacological Inhibition of VDCCs Suppresses IAV Replication, IAV Internalization, and IAV-Induced Ca^{2+} Oscillations.

(**A**, **B**) Replication of PR8 (**A**) or Aichi (**B**) in the absence (–) or presence of the indicated agents was determined with an MDCK cell plaque assay. Data are means ± s.e.m. ($n = 3$). *$P < 0.01$, **$P < 0.001$ versus nontreated cells, as calculated by one-way ANOVA with Dunnett's post-test. PFU, plaque-forming units.

(**C**) Effect of diltiazem on PR8 infection in the indicated cell lines as evaluated with an immunofluorescence-based assay. Data are means ± s.e.m. ($n = 3$). *$P < 0.05$, **$P < 0.001$ versus nontreated cells, as calculated by Student's *t* test. NP, nucleoprotein.

(**D**, **E**) Effect of diltiazem on PR8-induced Ca^{2+} oscillations in Cos-1 cells monitored with the FRET-based Ca^{2+} sensor YC3.60. FRET/CFP (cyan fluorescent protein) ratio images are shown in intensity-modified display (IMD) mode, and the upper and lower limits of the ratio range are indicated. Bar, 10 μm (**D**). Representative traces for the normalized FRET/CFP emission ratio are shown in **E**.

(**F**, **G**) Effect of diltiazem on PR8 internalization in Cos-1 cells as evaluated with an immunofluorescence-based assay. Representative images are shown. Boxed regions on the left are shown at higher magnification on the right. Bar, 10 μm (**F**). Rab7- and NP-positive regions were extracted and their co-localization was determined (**G**). Data are means ± s.e.m. ($n > 28$). *$P = 0.013$ versus nontreated cells, as calculated by Student's *t* test. See also Figure S1 and Supplementary Movies 1, 2.

Figure 2. Knockdown of $Ca_v1.2$ Inhibits IAV-Induced Ca^{2+} Oscillations, IAV Internalization, and IAV Infection.

(**A**) A549 cells were transfected first with an siRNA specific for $Ca_v1.2$ mRNA (siCav1.2#2 or -#13) or with a scrambled siRNA (siControl) for 48 h and then with an expression vector encoding YC3.60 for 24 h. The cells were then monitored by dual-emission microscopy with exposure to PR8 at time 0. Representative traces for the normalized emission ratio are shown.

(**B**, **C**) A549 cells transfected with siRNAs as in **A** were examined for PR8 internalization ($n > 40$) (**B**) and infection ($n > 5$) (**C**) with immunofluorescence-based assays. Data are means ± s.e.m. *$P < 1 \times 10^{-6}$ (**B**) or *$P < 0.002$ (**C**) versus control cells, as calculated by one-way ANOVA with Dunnett's post-test. See also Figure S2.

Figure 3. HA of IAV Binds to $Ca_v1.2$.

(**A**) Schematic representation of the membrane binding assay. IB, immunoblot analysis.

(**B**) Structure of $Ca_v1.2$ and sialylated asparagine residues in segment IV.

(**C**, **D**) Binding of PR8 to CFP-tagged full-length (FL) $Ca_v1.2$ in the absence or presence of sialidase (S) or EGTA (E) (**c**) or to the indicated FLAG epitope-tagged fragments of $Ca_v1.2$ (**D**) was examined with the membrane binding assay. Representative immunoblot analysis with antibodies to the M1 protein of IAV and to $Ca_v1.2$ (left) as well as quantitative data (means ± s.e.m., right) are shown. **P* = 0.016 versus nontreated cells (*n* = 4), as calculated by one-way ANOVA with Dunnett's post-test (**C**); **P* < 0.03 versus full-length $Ca_v1.2$ (*n* = 3), as calculated by one-way ANOVA with Dunnett's post-test (**D**). Arrowheads indicate bands corresponding to the expected sizes of the $Ca_v1.2$ fragments.

(**E**–**F**) Co-immunoprecipitation analysis of the binding of a 6×His-tagged form of HA (HA-His) to full-length (**E**) or fragments of (**F**) of $Ca_v1.2$ in 293T cells. CFP- or FLAG-tagged forms of $Ca_v1.2$ were immunoprecipitated (IP) with antibodies to green fluorescent protein (GFP) or to FLAG, respectively. Representative immunoblot analysis and quantitative data for co-immunoprecipitated HA-His (means ± s.e.m., *n* = 3) are shown. **P* < 0.04 versus wild-type $Ca_v1.2$, as calculated by one-way ANOVA with Dunnett's post-test. Arrowheads indicate bands corresponding to the expected sizes of the $Ca_v1.2$ fragments. See also Figure S3.

Figure 4. Glycosylation of $Ca_v1.2$ at Asn1436 or Asn1487 is Critical for IAV Infection.

(**A**) Co-immunoprecipitation analysis of the binding of a 6×His-tagged form of HA (HA-His) to glycosylation-deficient mutants of $Ca_v1.2$ in 293T cells. CFP- or FLAG-tagged forms of $Ca_v1.2$ were immunoprecipitated (IP) with antibodies to GFP or to FLAG, respectively. Representative immunoblot analysis and quantitative data for co-immunoprecipitated HA-His (means ± s.e.m., *n* = 3) are shown. **P* < 0.04 versus wild-type $Ca_v1.2$, as calculated by one-way ANOVA with Dunnett's post-test. Arrowheads indicate bands corresponding to the expected sizes of the $Ca_v1.2$ fragments.

(**B**) A549 cells transfected with $Ca_v1.2$ or control siRNAs were further transfected with expression vectors for wild-type or a glycosylation-deficient mutant of $Ca_v1.2$ and were then subjected to an immunofluorescence-based assay of PR8 infection. Data are means ± s.e.m. (*n* = 3). **P* < 0.05 versus control cells as calculated by one-way ANOVA with Dunnett's post-test. See also Figure S4.

Figure 5. Immunohistochemical Examination of IAV-Infected Mice

Representative pathological images of the nasal cavity (**A**), tracheae (**B**), and lungs (bronchiole (**C**) and alveoli (**D**)) of PR8 infected mice with hematoxylin and eosin staining (H & E; left panels), with immunohistochemistry for Ca_v (middle panels), and IAV NP (right panels). The lower panels in each subpanel were higher magnification images of the upper images. Bar, 50 μm.

Figure 6. The CCB Diltiazem Inhibits IAV Replication *In Vivo*.

(**A**) Protocol for *in vivo* experiments.

(**B**, **C**) The effect of prophylactic (**B**) or therapeutic (**C**) administration of diltiazem on IAV replication was evaluated by measurement of infectious virus particles in nasal lavage fluid and was compared with that of oseltamivir. Data are means ± s.e.m. ($n > 3$). *$P < 1 \times 10^{-4}$ (**B**) or *$P < 0.001$ (**C**) versus nontreated animals, as calculated by one-way ANOVA with Dunnett's post-test. A.U., arbitrary units.

(**D, E**) The effect of diltiazem on survival and body weight of mice infected with IAV. Mice were prophylactically administrated as in (**A**) and then infected with a sublethal dose of PR8 (10^4 PFU). Survival rate (**D**) and changes in body weight (**E**) were monitored for 14 days after infection. ($n = 6$). *P* values versus nontreated animals, as calculated by one-way ANOVA with log rank test (**D**) or Mauchly's sphericity test (**E**), are indicated in the graphs. See also Figure S5.

STAR METHODS

CONTACT FOR REAGENT AND RESOURCE SHARING

Further information and requests for resources and reagents should be directed to and will be fulfilled by the Lead Contact, Yusuke Ohba (yohba@med.hokudai.ac.jp).

EXPERIMENTAL MODEL AND SUBJECT DETAILS

Mice

Mouse experiments were approved and conducted in accordance with the guidelines established by the Hokkaido University Committee and National Institute of Infectious Diseases on Animal Care and Use. Male C57BL/6J or female BALB/c mice were housed under specific pathogen–free conditions at 21°C and 31% humidity. At least four mice for each group at 6–8 weeks of age were subjected to experiments.

Cell lines

Cos-1 (JCRB9082), HEK293T (ATCC CRL-11268), HeLa (CCL-2), A431 (CRL-1555), A549 (CCL-185), and BEAS-2B (~~ATCC~~ CRL-9609) cells were maintained under a humidified atmosphere of 5% CO_2 at 37°C in Dulbecco's modified Eagle's medium (DMEM) supplemented with 10% fetal bovine serum (Thermo Fisher Scientific), whereas MDCK cells (CCL-34) were maintained in minimum essential medium (MEM) (Sigma-Aldrich) supplemented with 10% fetal bovine serum. Expression vectors were introduced into cells by transfection with the use of Polyethylenimine "Max" (Polysciences).

Purification of viruses

IAV strains A/Puerto Rico/8/34 (H1N1; PR8) and A/Aichi/2/68 (H3N2; Aichi) were propagated for 48 h at 37°C in the chorioallantoic cavity of 10-day-old embryonated chicken eggs. Alternatively, MDCK cells were infected with viruses at a multiplicity of infection (MOI) of 0.0001 plaque-forming unit (PFU) per cell for 48 h at 37°C. Viruses isolated by high-speed centrifugation were resuspended in phosphate-buffered saline and stored at –80°C until use. The amount of infectious virus in culture supernatants was determined with a plaque assay.

METHOD DETAILS

Plasmids.

Expression vectors for the FRET-based biosensor YC3.60 (Nagai et al., 2004) were kindly provided by A. Miyawaki (RIKEN). Human $Ca_v1.2$ cDNA was prepared from total RNA of 293T cells by reverse transcription (RT) and the polymerase chain reaction (PCR) with the primers CAV12_F and CAV12_R. The coding sequences for fragments I-II, I-III, I-IV and III-IV of $Ca_v1.2$ were amplified by PCR with the primers CAV12_F and II_R; CAV12_F and III_R; CAV12_F and IV_R; and III_F and IV_R, respectively. All PCR products were subcloned into the *Xho*I and *Not*I sites of the pCAGGS-Flag-IRES-ExRed or pFX-SECFP vectors (Fujioka et al., 2013; Horiguchi et al., 2017). The cDNAs encoding the N1436Q or N1487Q mutants of $Ca_v1.2$ were obtained by PCR-based mutagenesis with the use of a QuikChange Site-Directed Mutagenesis Kit (Agilent Technologies) and with the primer pairs N1436Q_F and N1436Q_R or N1487Q_F and N1487Q_R.

To generate plasmids encoding the target sequences of $Ca_v1.1$–$Ca_v1.4$ for quantitative PCR (qPCR), the cDNA of 293T cells were amplified with primers Cav1.1-F and Cav1.1-R, Cav1.2-F and Cav1.2-R, Cav1.3-F and Cav1.3-R, as well as Cav1.4-F and Cav1.4-R, and the resulting PCR products were subcloned into pCR-Blunt II-TOPO (Thermo Fisher Scientific).

cDNA for HA of PR8 was a kind gift from K. Kihatsu (Osaka University) and its coding sequence was amplified by PCR with the primers PR8HA_F and PR8HA_R and was subcloned into the *Eco*RI and *Xho*I sites of a modified pCA7 vector (Takeda et al., 2005). The encoded protein consists of HA1, the ectodomain of HA2, foldon (a natural trimerization domain of T4 bacteriophage fibritin) (Meier et al., 2004), and a 6×His tag (**Figure S3D**).

cDNA for Sirius was kindly provided by T. Nagai (Osaka University; (Tomosugi et al., 2009) and its coding sequence was amplified by PCR with the primers Sirius_F and Sirius_R and was subcloned into the *Xho*I and *Not*I sites of pFX-CAAX (Fujioka et al., 2013; Horiguchi et al., 2017).

Cytotoxicity assay

Cells were cultured in 96 well plates in the absence or presence of CCBs or BAPTA-AM for 48 h (**Figure S1B**) or for 6 h (**Figure S1F**), fixed with 3% paraformaldehyde, and then stained with Gram's crystal violet solution (Merck). The cells were washed with distilled water and air-dried. The absorbance at 590 nm was measured by the SpectraMax i3x Multi-Mode microplate reader (Molecular Devices), based on which cell viability (or cytotoxicity of drugs) was determined.

Fluorescent labeling of viruses

For preparation of fluorescently labeled PR8, 1 ml of purified virus suspension (0.4 mg/ml) was incubated with 100 μM DiD stock solution in the dark for 1 h at room temperature (Nanbo et al., 2010).

Plaque assay

A plaque assay was performed as described previously (Pleschka et al., 2001; Yoshida et al., 2009). In brief, confluent monolayers of MDCK cells in 12-well plates were inoculated with the conditioned medium of virus-infected cells or directly with virus suspension. After culture for 1 h, the culture supernatants were removed and the cells were overlaid with MEM containing 1% Bacto-agar and trypsin (5 μg/ml). Plaques were counted after incubation of the cells at 35°C under 5% CO_2 for 2 days.

Immunofluorescence-based virus internalization and infection assays

Immunofluorescence-based virus internalization and infection assays were performed as described previously (Fujioka et al., 2013). In brief, serum-deprived cells were either treated with inhibitors for 30 min or left untreated and then incubated with IAV at an MOI of 10 PFU per cell for 1 h (internalization assay) or at an MOI of 1 PFU per cell for 4 h (infection assay). Cells were then fixed with 3% paraformaldehyde for 15 min at room temperature, permeabilized with 0.1% Triton X-100 in phosphate-buffered saline for 4 min at room temperature and then incubated with 1% bovine serum albumin to block nonspecific binding of antibodies. The cells were further incubated with primary antibodies (NP, 1:1,000 dilution; Rab7, 1:250 dilution) overnight at 4°C, after which immune complexes were detected by incubation for 1 h at room temperature in the dark with AlexaFluor488-, AlexaFluor594- or AlexaFluor647-conjugated secondary antibodies (1:250 dilution). Nuclei were visualized by staining with Hoechst 33342. Images were acquired with an FV-10i confocal microscope (Olympus) for the internalization assay or with a wide-field fluorescence microscope (IX-81, Olympus) for the infection assay.

For analysis of virus internalization, confocal sections (with a *z* step of 0.2 μm) were acquired from the bottom to the top of cells and subjected to background subtraction. Vesicles positive for NP or Rab7 were extracted with the use of the ‘granularity’ module of MetaMorph software (SCR_002368, Universal Imaging), and the co-localization of NP with Rab7 was quantified with the ‘measure co-localization’ function. For analysis of virus infection, the fluorescence intensity of NP in the nucleus was measured and the percentage of NP-positive cells was determined.

Fluorescence microscopy and FRET analysis

FRET imaging and data analysis were performed essentially as described previously (Fujioka et al., 2013; Ohba et al., 2003). In brief, cells were transfected with a vector for YC3.60 for 24 h, deprived of serum for 4 h and placed in a stage-top incubation chamber (Live Cell Instrument) at 37°C on an Olympus IX-81 microscope equipped with a BioPoint MAC6000 filter and shutter control unit (Ludl Electronic Products), an automated XY-stage (Chuo Precision Industrial) and a Cool SNAP MYO cooled charge-coupled device camera (Photometrics). Cells were illuminated with a SOLA Light Engine (Lumencor) through an FF02-438/24 excitation filter (Semrock), and cyan fluorescent protein (CFP) and FRET fluorescence images obtained through FF01-483/32 and FF01-542/27 emission filters (Semrock), respectively, were recorded every 30 s. After 10 to 15 min, the cells were infected with IAV at an MOI of 1 PFU per cell. In some experiments, cells were exposed to inhibitors for 30 min before infection. FRET efficiency (FRET/CFP emission ratio) was calculated as the quotient of background-subtracted FRET and CFP images and was presented in an intensity-modified display (IMD) mode with MetaMorph software. Eight colors from red to blue were used to represent the emission ratio, with the intensity of each color indicating the mean intensity of FRET and CFP as indicated.

To determine the cell surface expression levels of VDCCs, 293T cells were transfected with expression vectors for either wild-type form, truncation form, or glycosylation-deficient mutant form of FLAG-tagged $Ca_v1.2$, along with that for Sirius-CAAX (marker for plasma membrane) for 24h. The cells were then subjected to immunofluorescence with the use of an anti-FLAG antibody. Mask images for plasma membrane were generated by binary images of Sirius-CAAX, whereas those for entire cell area were generated by filling the inside of CAAX-positive region. Fluorescence intensities in the plasma membrane region and entire cell region were thereby quantified, assumed as the expression level of $Ca_v1.2$ in each region, and plotted.

Immunoblot analysis

Unless otherwise specified, cells were lysed in lysis buffer (50 mM Tris-HCl (pH 7.4), 150 mM NaCl, 0.25% Fos-choline, 1 mM $CaCl_2$, 1 mM $MgCl_2$, 1 mM phenylmethylsulphonyl fluoride, 1 mM Na_3VO_4, cOmplete Protease Inhibitor Cocktail (Sigma-Aldrich)) for 30 min on ice. The lysates were centrifuged at 20,000 × *g* for 10 min at 4°C, and the resulting supernatants were subjected to SDS-polyacrylamide gel electrophoresis. The separated proteins were transferred to a polyvinylidene difluoride membrane (Bio-Rad) and subjected to

immunoblot analysis. Immune complexes were detected with the use of ECL Western Blotting Detection Reagent (GE Healthcare) and an LAS-1000UVmini image analyzer (Fujifilm).

Immunoprecipitation

Cells were lysed and the lysates centrifuged as described for immunoblot analysis, and the resulting supernatants were incubated with primary antibodies for 1 h at 4°C with gentle rotation before the addition of protein G– or protein A–Sepharose beads (GE Healthcare) and further incubation for 1 h. The bead-bound immune complexes were isolated by centrifugation, washed twice with lysis buffer, eluted in SDS sample buffer and subjected to immunoblot analysis.

Membrane binding assay

293T cells were transfected for 24 h with expression vectors for full-length or fragments of $Ca_v1.2$ and then resuspended in Tris-buffered saline containing 1 mM Na_3VO_4. A membrane fraction of the cells was prepared by freeze-thawing and subsequent centrifugation at 20,400 × *g* for 10 min at 4°C and was incubated for 12 h at 4°C in a 96-well plate coated with antibodies to $Ca_v1.2$ (AB_2039771, Alomone Labs). After washing with Tris-buffered saline containing 1 mM Na_3VO_4, the wells of the plate were further incubated with PR8 for 1 h at 4°C. After extensive washing, the material adsorbed to each well was eluted in SDS sample buffer and subjected to immunoblot analysis.

RNA interference

The siRNAs targeting human $Ca_v1.2$ mRNA (siCav1.2#2, Hs_Cav1.2_2; siCav1.2#13, Hs_Cav1.2_13) were obtained from Qiagen and were introduced into cells by transient transfection with the use of the Lipofectamine RNAiMax reagent (Thermo Fisher Scientific). AllStars Negative Control siRNA (Qiagen) was used as a control.

RNA isolation, RT and quantitative PCR analysis

Total RNA was isolated from cells with the use of an RNeasy Mini Kit (Qiagen), and portions of the RNA (2.0 μg) were subjected to RT with SuperScript VILO reverse transcriptase (Thermo Fisher Scientific). Quantitative PCR analysis was performed with the use of a StepOne real-time PCR system (Thermo Fisher Scientific) and the following primers: Cav1.1-F and Cav1.1-R, Cav1.2-F and Cav1.2-R, Cav1.3-F and Cav1.3-R, Cav1.4-F and Cav1.4-R. The copy number of each Ca^{2+} channel was then determined by extrapolation from a calibration curve that was obtained by qPCR with calibrator plasmids as a template.

3D culture

BEAS-2B cells (3×10^4) were cultured on or in Matrigel (BD-Discovery Labware) in a 35 mm glass-based dish for 5 days. After confirming monolayer or spheroid formation, the cells were further cultured in the presence of absence of diltiazem for 2 h, exposed to PR8 at an MOI of 1 PFU/cell, and subjected to immunofluorescence with the use of antibodies to IAV NP and $Ca_v1.2$. Nuclei were counterstained with Hoechst33342. The samples were observed under confocal microscopy.

Animal experiments

Six-week-old male C57BL/6J mice and eight-week-old female BALB/c mice were infected by direct delivery of PR8 ($50–3 \times 10^4$ PFU) to the nares with a micropipette under isoflurane anesthesia, as described previously (Edenborough et al., 2012; Ng et al., 2010). The mice were housed separately for 3 days after virus exposure. Diltiazem (10 or 20 mg/kg/day) or oseltamivir (40 mg/kg/day) was administered intranasally or intraperitoneally beginning either 1 day before or 1 day after virus exposure. Nasal lavage fluid was collected 3 days after virus exposure and was assayed for the amount of infectious virus with the immunofluorescence-based infection assay. To monitor survival and body weight changes at lethal dose of IAV infection, at least six mice were infected with PR8 (10^4 PFU) as described above. The mice were housed and monitored separately for 14 days after virus exposure. Diltiazem (20 mg/kg/day) or oseltamivir (40 mg/kg/day) was administered intranasally or intraperitoneally, respectively, beginning 1 day before virus exposure.

To perform immunohistochemical experiments, mice were euthanized at 2 days post-infection. Excised tissues preserved in 4% paraformaldehyde for 12 h were subsequently processed for paraffin embedding and cut into 3-μm-thick sections. One section from each tissue sample was stained using a standard hematoxylin and eosin procedure, and the others were subjected to immunohistochemistry. For visualization of replicated influenza viruses, a rabbit polyclonal NP antibody (Iwasaki et al., 1999) was used as a primary antibody after heat-mediated antigen retrieval in citrate buffer at 121ºC for 10 min. Immunohistochemistry for Ca_v proteins was performed with a rabbit polyclonal anti-panCa_v α antibody (AB_2039762, Alomone Labs) as a primary antibody after antigen retrieval in 0.025% trypsin solution at 37ºC for 30 min. A peroxidase-labeled polymer-conjugated anti-rabbit immunoglobulin (Dako) was used as a secondary antibody. Immune complexes were visualized by means of 3,3’-diaminobenzidine tetrahydrochloride staining. Hematoxylin (Modified Mayer’s) was used as a nuclear counterstain.

QUANTIFICATION AND STATISTICAL ANALYSIS

Quantitative data are presented as means ± s.e.m. from at least three independent experiments (unless indicated otherwise) and were compared by Student's *t* test (between two conditions) or by one-way analysis of variance (ANOVA) followed by Dunnett's post-hoc analysis (among multiple conditions), log rank test (**Figure 6D**) or Mauchly's sphericity test (**Figure 6E**).

SUPPLEMENTARY INFORMATION

Supplemental Movie 1. Representative Video Images of IAV-Induced Ca^{2+} Oscillations (Related to Figures 1D and E).

Cos-1 cells expressing YC3.60 were monitored by dual-emission, time-lapse microscopy with exposure to PR8. The upper and lower limits of the emission ratio in IMD mode were set to 4.0 and 2.8, respectively.

Supplemental Movie 2. Representative Video Images of IAV-Induced Ca^{2+} Oscillations in The Presence of Diltiazem (Related to Figures 1D and E).

Cos-1 cells expressing YC3.60 were treated with diltiazem and then monitored by dual-emission, time-lapse microscopy with exposure to PR8. The upper and lower limits of the emission ratio in IMD mode were set to 4.0 and 2.8, respectively.

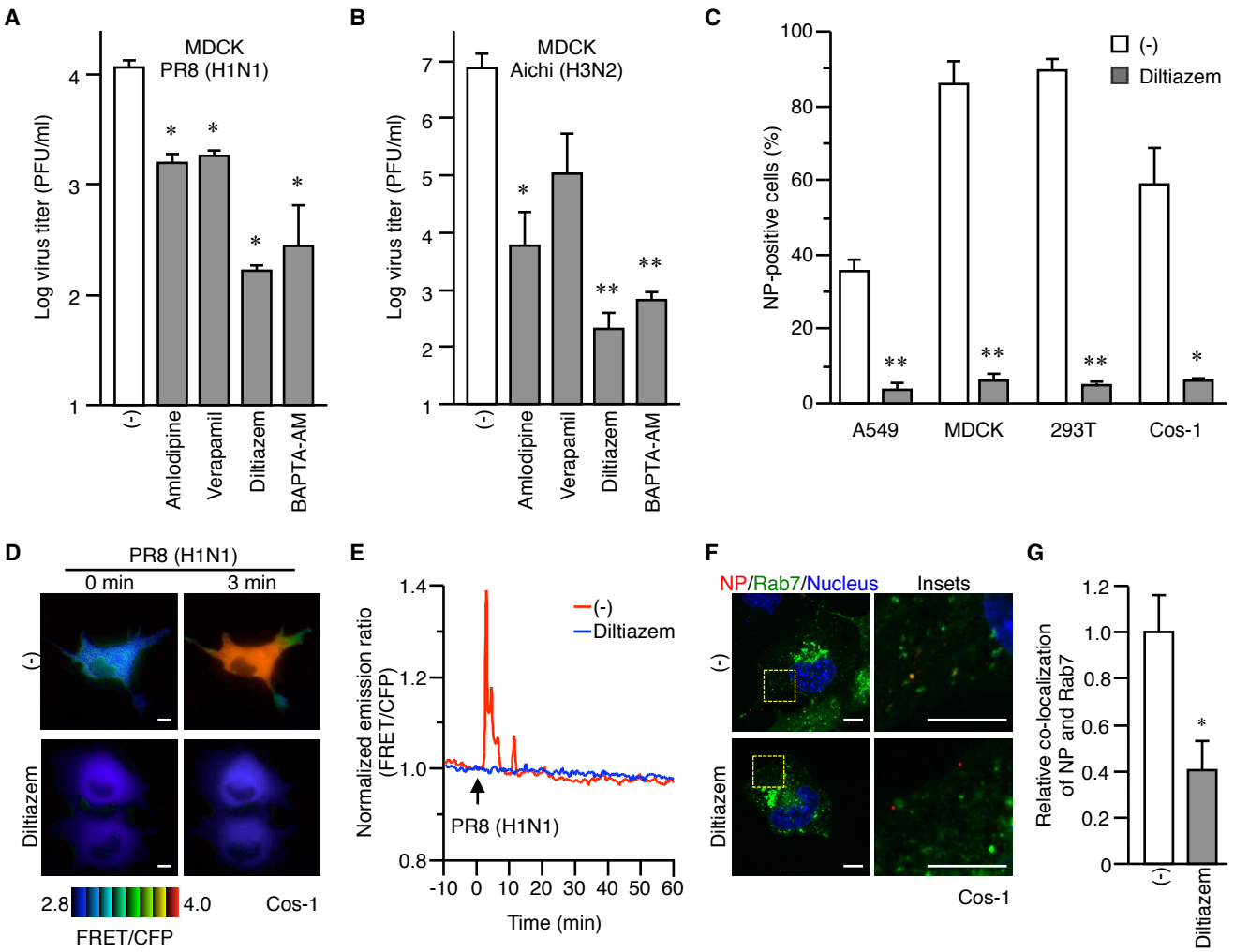
A
MDCK
PR8 (H1N1)
Log virus titer (PFU/ml)
(-)
Amlodipine
Verapamil
Diltiazem
BAPTA-AM
B
MDCK
Aichi (H3N2)
Log virus titer (PFU/ml)
C
NP-positive cells (%)
(-)
Diltiazem
A549
MDCK
293T
Cos-1
D
PR8 (H1N1)
0 min
3 min
(-)
Diltiazem
2.8
4.0
FRET/CFP
Cos-1
E
Normalized emission ratio (FRET/CFP)
(-)
Diltiazem
PR8 (H1N1)
Time (min)
F
NP/Rab7/Nucleus
Insets
(-)
Diltiazem
Cos-1
G
Relative co-localization of NP and Rab7
(-)
Diltiazem

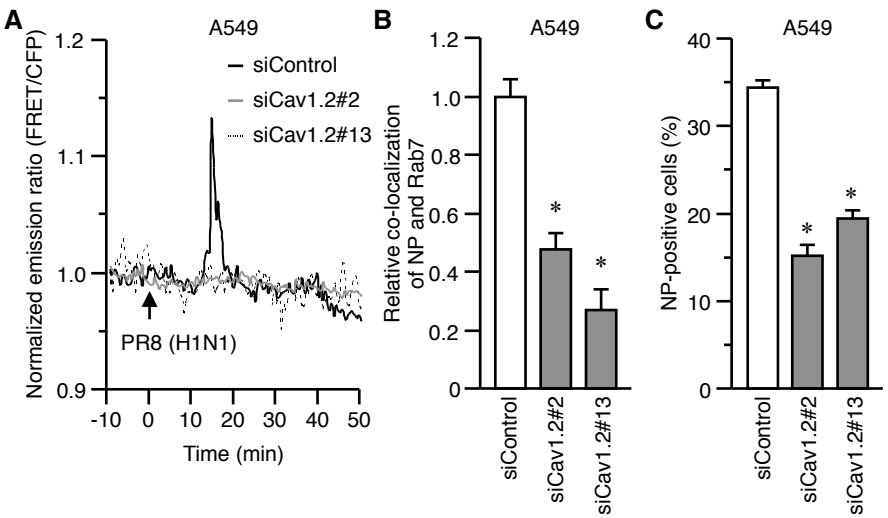

Y. Fujioka, et al., Figure 2

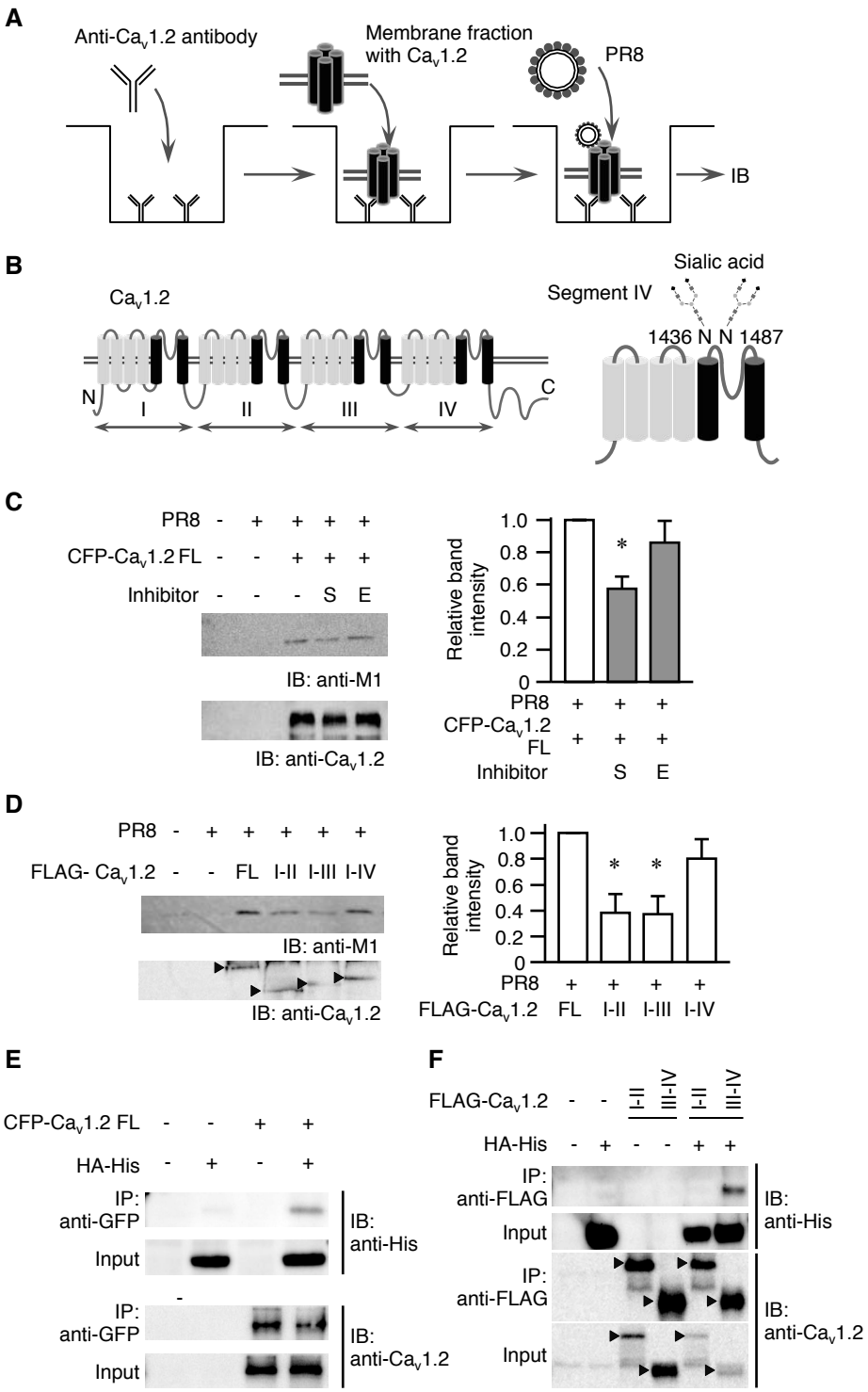

Y. Fujioka, et al., Figure 3

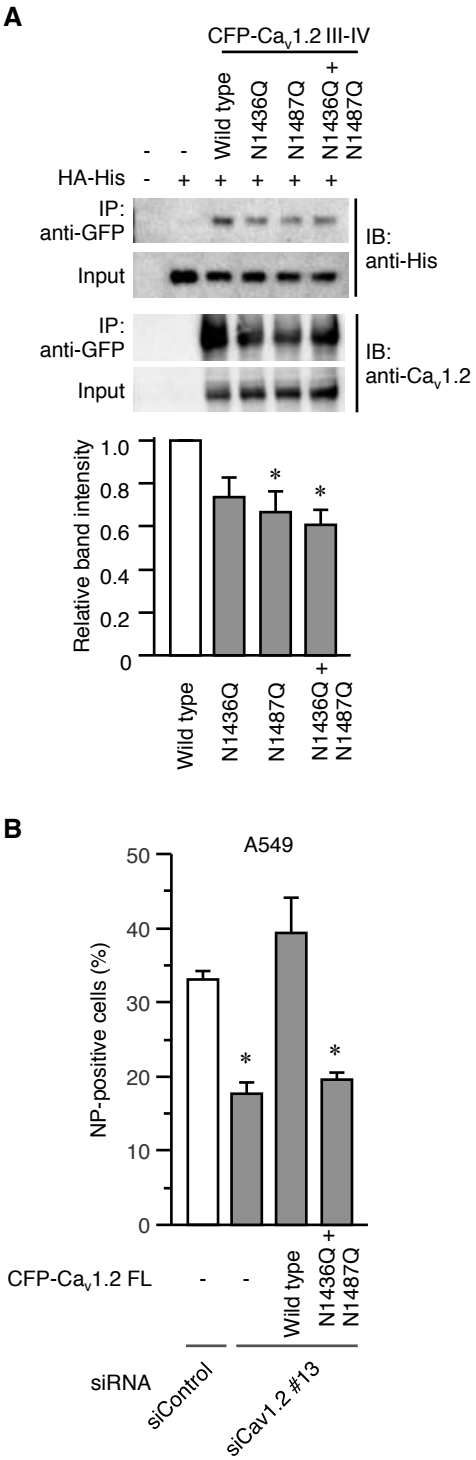
A
CFP-Cav1.2 III-IV
Wild type
N1436Q
N1487Q
N1436Q + N1487Q
HA-His
IP: anti-GFP
Input
IB: anti-His
IB: anti-Cav1.2
Relative band intensity
1.0
0.8
0.6
0.4
0.2
0
*
B
A549
NP-positive cells (%)
50
40
30
20
10
0
CFP-Cav1.2 FL
siRNA
siControl
siCav1.2 #13

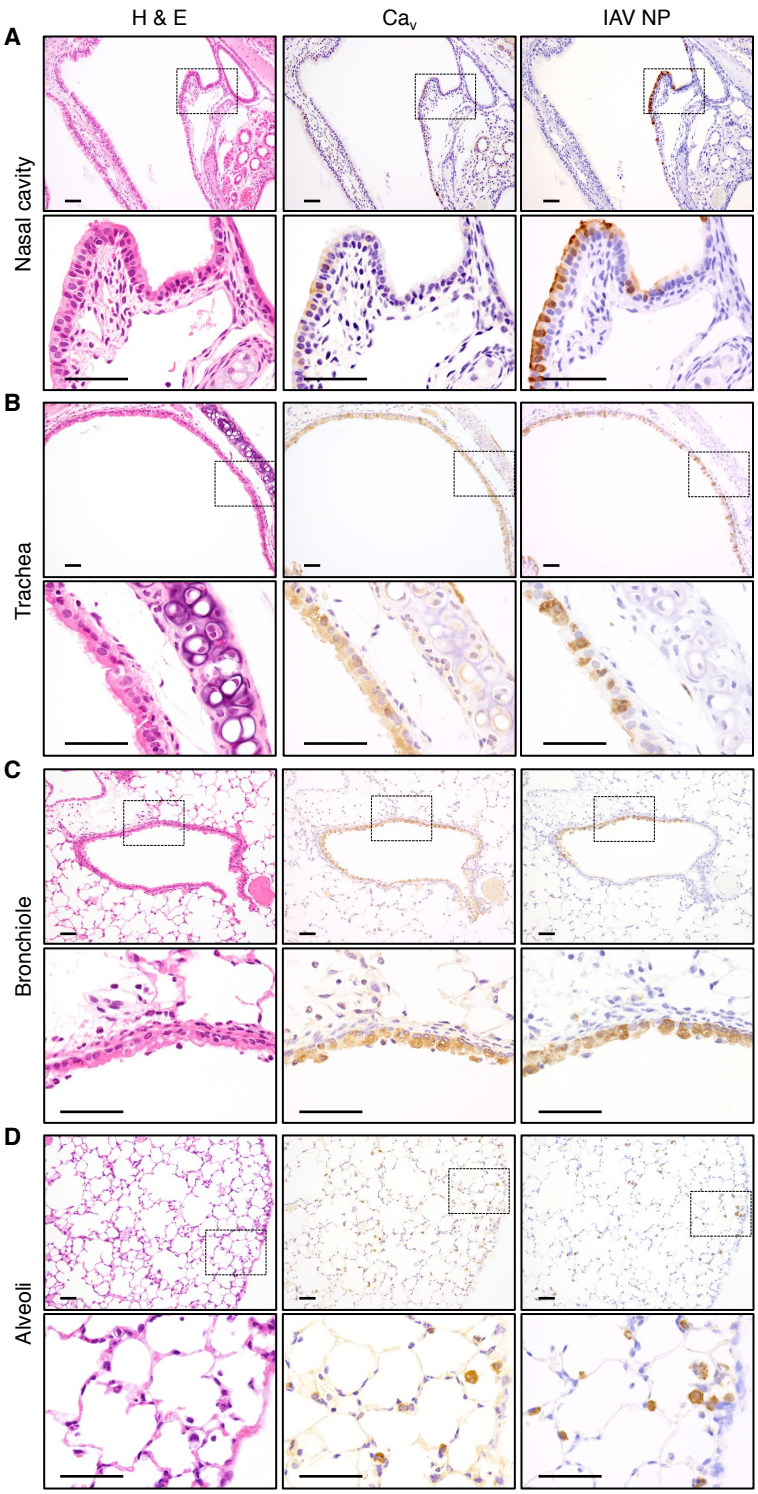

Y. Fujioka, et al., Figure 5

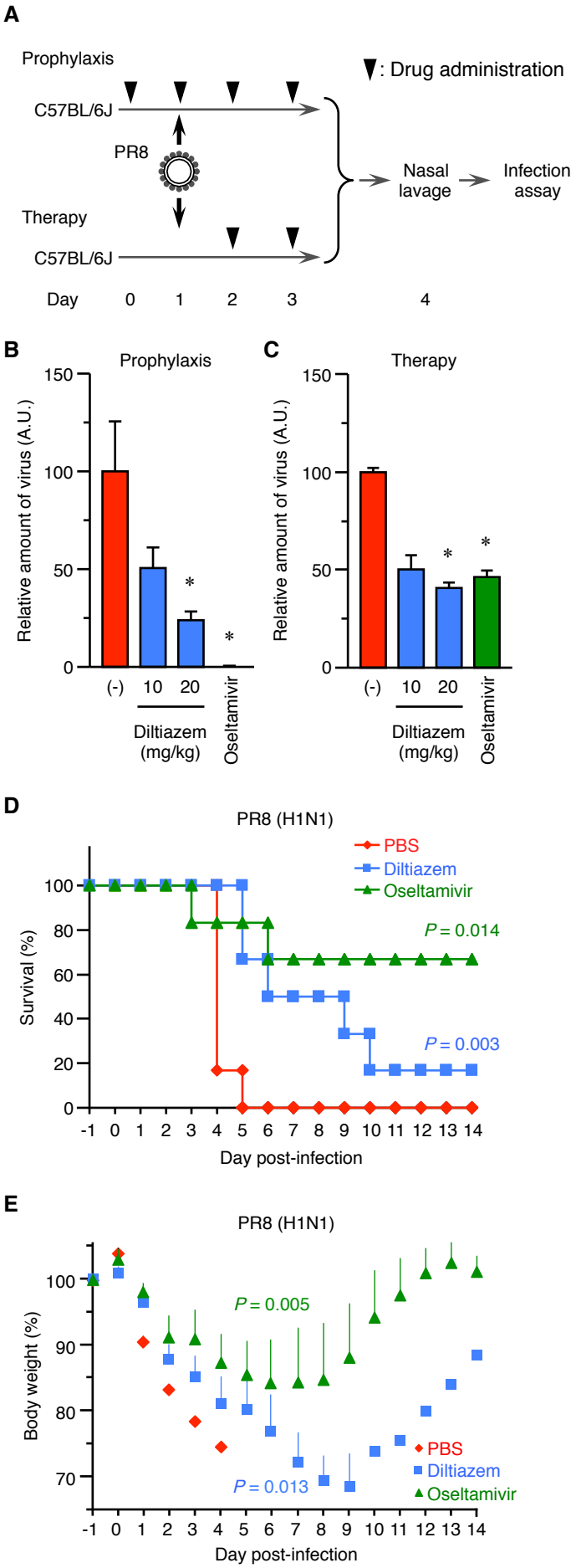

Y. Fujioka, et al., Figure 6

KEY RESOURCES TABLE

REAGENT or RESOURCE	SOURCE	**IDENTIFIER**
Antibodies		
Mouse monoclonal anti-NP	Abcam	**Cat#ab20343; RRID: AB_445525**
Rabbit polyclonal anti-NP	Iwasaki et al., 1999	**N/A**
Rabbit polyclonal anti-$Cav_{1.2}$	Alomone Labs	**Cat#ACC-003; RRID: AB_2039771**
Rabbit polyclonal anti-panCav α	Alomone Labs	**Cat#ACC-004; RRID: AB_2039762**
Mouse monoclonal anti-GFP	Medical & Biological Laboratories	**Cat#D153-3; RRID: AB_591817**
Rabbit polyclonal GFP	Medical & Biological Laboratories	**Cat#598; RRID: AB_591819**
Mouse monoclonal anti-6×His	Medical & Biological Laboratories	**Cat#D291-3; RRID: AB_10597733**
Mouse monoclonal anti-Rab7 (D95F2)	Cell Signaling Technology	**Cat#9367S; RRID: AB_1904103**
Mouse monoclonal anti-β-actin	Santa Cruz Biotechnology	**Cat#sc-47778; RRID: AB_626632**
Mouse monoclonal anti-FLAG (M2)	Sigma-Aldrich	**Cat#F1804; RRID: AB_262044**
AlexaFluor488-conjugated goat anti-mouse IgG	Thermo Fisher Scientific	**Cat#A-11029; RRID: AB_2534088**
AlexaFluor594-conjugated donkey anti-rabbit IgG	Thermo Fisher Scientific	**Cat#A-21207; RRID: AB_141637**
AlexaFluor647-conjugated chicken anti-rat IgG	Thermo Fisher Scientific	**Cat#A21472; RRID: AB_2535875**
HRP-conjugated goat anti-mouse IgG	Biosource	**Cat#AMI0404**
HRP-conjugated goat anti-rabbit IgG	Biosource	**Cat#ALI0404**
HRP-conjugated donkey anti-goat IgG	Promega	**Cat#V8051; RRID: AB_430838**
Peroxidase-labeled polymer-conjugated anti-rabbit IgG (EnVision/HRP)	Dako	**Cat#K4003; RRID: AB_2630375**
Bacterial and Virus Strains		
A/Puerto Rico/8/34 (H1N1; PR8)	Fujioka et al., 2013	**N/A**
A/Aichi/2/68 (H3N2; Aichi)	Fujioka et al., 2013	**N/A**
Biological Samples		
Mouse respiratory tissue specimen (paraformaldehyde-fixed, paraffin-embedded)	This paper	**N/A**
Chemicals, Peptides, and Recombinant Proteins		
Hoechst 33342	Thermo Fisher Scientific	**Cat#H3570; CAS: 23491-52-3**
DiD	Thermo Fisher Scientific	**Cat#D7757; CAS: 127274-91-3**
The acetoxymethyl ester of 1,2-bis(2-aminophenoxy)ethane-*N*,*N*,*N*',*N*'-tetraacetic acid (BAPTA-AM, 25 μM, otherwise specified)	Sigma-Aldrich	**Cat#A-1076; CAS: 126150-97-8**
EGTA (1 mM)	Sigma-Aldrich	**Cat#E-4378; CAS: 67-42-5**

sialidase of *Vibrio Cholera* (5 mU/ml)	Sigma-Aldrich	**Cat#N7885; CAS: 9001-67-6**
amlodipine (25 μM, otherwise specified)	Sigma-Aldrich	**Cat#A5605; CAS: 111470-99-6**
verapamil (50 μM, otherwise specified)	Sigma-Aldrich	**Cat#V4629; CAS: 152-11-4**
diltiazem (200 μM, 10 or 20 mg/kg, otherwise specified)	Sigma-Aldrich	**Cat#D2521; CAS: 33286-22-5**
Oseltamivir phosphate (40 mg/kg)	CAYMAN	**Cat#16070; CAS: 204255-11-8**
PNGase F (25 U/μl)	New England Biolabs	**Cat#P0704S**
Polyethylenimine "Max"	Polysciences	**Cat#POL 24765; CAS: 49553-93-7**
cOmplete Protease Inhibitor Cocktail	Sigma-Aldrich	**Cat#11697498001**
protein G–Sepharose	GE Healthcare	**Cat#17061801**
protein A–Sepharose	GE Healthcare	**Cat#17528001**
Fos-Choline	Anatrace	**Cat#F308; CAS: 29557-51-5**
Lipofectamine RNAiMax reagent	Thermo Fisher Scientific	**Cat#13778-150**
Gram's crystal violet solution	Merck	**Cat#1.09218.0500**
Matrigel	BD-Discovery Labware	**Cat#256237**
Critical Commercial Assays		
RNeasy Mini Kit	Qiagen	**Cat#74104**
SuperScript VILO cDNA Synthesis Kit	Thermo Fisher Scientific	**Cat#11754-050**
StepOne real-time PCR system	Thermo Fisher Scientific	**N/A**
Experimental Models: Cell Lines		
Cos-1	JCRB	**JCRB9082**
HEK293T	ATCC	**CRL-11268**
HeLa	ATCC	**CCL-2**
A431	ATCC	**CRL-1555**
A549	ATCC	**CCL-185**
MDCK	ATCC	**CCL-34**
BEAS-2B	ATCC	**CRL-9609**
Experimental Models: Organisms/Strains		
Mouse: Male C57BL/6J at 6 weeks of age	CLEA	**N/A**
Mouse: Female BALB/c at 8 weeks of age	Japan SLC inc.	**N/A**
Oligonucleotides		
See Table S1 for primers used for cloning and qPCR	This paper	**Table S1**
siRNA targeting sequence: siCav1.2#2: Hs_Cav1.2_2	Qiagen	**Cat#SI00337176**
siRNA targeting sequence: siCav1.2#13: Hs_Cav1.2_13	Qiagen	**Cat#SI04948237**
AllStars Negative Control siRNA	Qiagen	**Cat#SI03650318**
Recombinant DNA		
YC3.60	Nagai et al., 2004	**N/A**
pCAGGS-Flag-IRES-ExRed-Cav1.2	This paper	**N/A**
pCAGGS-Flag-IRES-ExRed-Cav1.2 I-II	This paper	**N/A**
pCAGGS-Flag-IRES-ExRed-Cav1.2 I-III	This paper	**N/A**

pCAGGS-Flag-IRES-ExRed-Cav1.2 I-IV	This paper	**N/A**
pCAGGS-Flag-IRES-ExRed-Cav1.2 III-IV	This paper	**N/A**
pCAGGS-Flag-IRES-ExRed-Cav1.2 III-IV N1436Q	This paper	**N/A**
pCAGGS-Flag-IRES-ExRed-Cav1.2 III-IV N1487Q	This paper	**N/A**
pCAGGS-Flag-IRES-ExRed-Cav1.2 III-IV N1436/1487Q	This paper	**N/A**
pCAGGS-Flag-IRES-ExRed-Cav1.2 N1436/1487Q	This paper	**N/A**
pFX-SECFP-Cav1.2	This paper	**N/A**
pFX-SECFP-Cav1.2 I-II	This paper	**N/A**
pFX-SECFP-Cav1.2 III-IV	This paper	**N/A**
pFX-SECFP-Cav1.2 III-IV N1436Q	This paper	**N/A**
pFX-SECFP-Cav1.2 III-IV N1487Q	This paper	**N/A**
pFX-SECFP-Cav1.2 III-IV N1436/1487Q	This paper	**N/A**
pFX-SECFP-Cav1.2 N1436/1487Q	This paper	**N/A**
pCA7-HA-His	This paper	**N/A**
pFX-Sirius-CAAX	This paper	**N/A**
pCR-Blunt II-TOPO-Cav1.1 qPCR	This paper	**N/A**
pCR-Blunt II-TOPO-Cav1.2 qPCR	This paper	**N/A**
pCR-Blunt II-TOPO-Cav1.3 qPCR	This paper	**N/A**
pCR-Blunt II-TOPO-Cav1.4 qPCR	This paper	**N/A**
Software and Algorithms		
MetaMorph	Molecular Devices	**RRID: SCR_002368**